

2-D Transient Numerical Code for Hybrid Rocket Simulations with Detailed Chemistry

Alexandre Mangeot¹

*PRISME Laboratory, 63 avenue de Lattre de Tassigny, 18000 Bourges, France
CNES, Rond Point de l'Espace, 91023 Evry Cedex, France*

Nicolas Gascoin², Philippe Gillard³

PRISME Laboratory, 63 avenue de Lattre de Tassigny, 18000 Bourges, France

Hybrid rocket technology is known since the 30's and it is covered by a large number of experimental, fundamental and applied research works. It still suffers from a lack of chemical description and of detailed numerical simulation of core phenomena. Several numerical codes have emerged to simulate hybrid rocket combustion chamber but with limited consideration for detailed chemistry. They generally use global Arrhenius law or tabulated regression rate to simulate the solid fuel pyrolysis and equilibrium calculation for the combustion. A new 2-D transient reactive numerical code is proposed in this paper with the use of detailed chemical mechanisms for both pyrolysis and combustion reactions (over 1000 species and 10000 reactions). The features of the numerical code are presented in this paper, as well as the equations used to model the physical and chemical phenomena. The simplification assumptions are presented and the code validation is proposed through analytical and numerical comparisons with bibliographic data on reference test cases. The heat transfer in solid phase has been validated with a 99,9% accuracy. The mass and heat transfer in the gas phase have shown a mass and energy conservation of around 99,7%. The gas flow has been validated also on the boundary layer with more than 99,5% accuracy. For chemistry phenomena, special treatment must be applied, leading to an error less than 2% on the ignition delay for combustion process.

Nomenclature

E_{ak}	=	Activation energy Arrhenius factor of the k^{th} reaction [$J.mol^{-1}$]
f_x, f_y	=	Body forces along the x and y directions [$m.s^{-2}$]
ρ	=	Density [$kg.m^{-3}$]
μ	=	Dynamic viscosity [$Pa.s$]
q_x, q_y	=	Heat fluxes along x and y directions [$W.m^{-2}$]
u	=	Internal specific energy [$J.kg^{-1}$]
j_{xi}, j_{yi}	=	Mass fraction fluxes of the i^{th} specie along the x and y directions [$m.s^{-1}$]
Y_i	=	Mass fraction of the i^{th} specie
D_{mi}	=	Mixture diffusion coefficient of the i^{th} specie [$m^2.s^{-1}$]
Mw_i	=	Molar weight of the i^{th} specie [$kg.mol^{-1}$]
p_{th}	=	Net power thermal density [$W.m^{-3}$]
$\dot{\omega}_i$	=	Net production rate [$kg.m^{-3}.s^{-1}$]
R	=	Perfect gas constant [$J.mol^{-1}.K^{-1}$]

¹ Main author: Alexandre.Mangeot@bourges.univ-orleans.fr, PhD Student

² Corresponding author: Nicolas.Gascoin@bourges.univ-orleans.fr, Associate Professor, AIAA Member

³ Full Professor

B_k	= Pre-exponential Arrhenius factor of the k^{th} reaction [$(\text{mol.m}^{-3})^{1-m}.\text{s}^{-1}$]
p	= Pressure [Pa]
R_k	= Specific reaction rate of the k^{th} reaction [$(\text{mol.m}^{-3})^{1-m}.\text{s}^{-1}$]
x, y	= Space variables [m]
c	= Specific heat capacity (for a solid) [$\text{J.kg}^{-1}.\text{K}^{-1}$]
c_{pi}	= Specific heat capacity at constant pressure of the i^{th} specie [$\text{J.kg}^{-1}.\text{K}^{-1}$]
c_v	= Specific mixture heat capacity at constant volume [$\text{J.kg}^{-1}.\text{K}^{-1}$]
c_v	= Specific mixture heat capacity at constant volume [$\text{J.kg}^{-1}.\text{K}^{-1}$]
$\Delta h_{f_i}^0$	= Standard heat of formation of the i^{th} specie [J.kg^{-1}]
$\nu_{i,k}$	= Stoichiometric factor of the i^{th} specie in the k^{th} reaction [$(\text{mol.m}^{-3})^{1-m}.\text{s}^{-1}$]
T	= Temperature [K]
α_k	= Temperature exponent Arrhenius factor of the k^{th} reaction
λ	= Thermal conductivity [$\text{W.m}^{-1}.\text{K}^{-1}$]
t	= Time [s]
v_x, v_y	= Velocity components along the x and y directions [m.s^{-1}]
$\tau_x, \tau_y, \tau_{xy}$	= Viscous stress tensor components [N.m^{-2}]

I. Introduction

A. Fundamental of Hybrid Rocket and past and current research activities

LIQUID and solid propellant rocket technologies dominate rocket propulsion field due to performance and technological maturity reasons. Hybrid technology involves (in its conventional configuration) a solid fuel stored in the combustion chamber that burns with the oxidizer injected either under liquid or gaseous phase. The heat flux of the combustion makes the solid fuel pyrolyze and this produces the gaseous fuel. By separating the propellants, the engine ought to become safer than a solid rocket. The solid fuel can be handled with less caution. It is even possible to adapt the thrust or to shut the engine down by controlling the injected oxidizer mass flow rate.

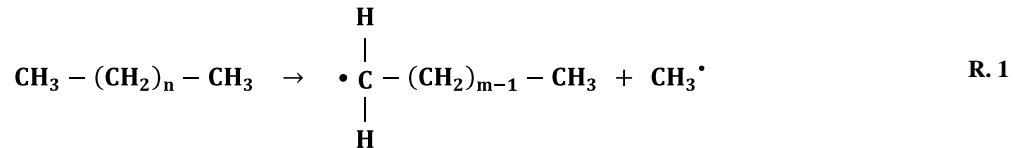
Nevertheless, hybrid rocket technology suffers from low performance (low regression rate, that is to say low gaseous fuel production) and its use remains rare. Since the 70s [1], numerous studies have been conducted around the world to improve this technology. The work has been focused on the design of swirl injectors [2,3], on the geometry of reducer grain [4,5], on the chemical formula of both oxidizer and reducer [6-8] and on additives to increase the reducer regression [9-11]. Recently the first flight of the SpaceShip One in 2004 propelled with a hybrid engine showed that the technology has potential for future commercial applications [1].

Numerous projects are currently under development on hybrid topics. Astrium company leads the European ORPHEE program which aims at determining the ability on hybrid engines, the possible applications and the requirements on regression rate for example [12]. The French space agency CNES also develops its own activity project (PERSEUS, French acronym for Student Project of Scientific and Academic European Space Research) in order to promote, among others, hybrid propulsion studies. In this framework, the Roxel company and the University of Orléans collaborate to a research work with CNES in order to develop a numerical code, which is able to handle detailed chemistry. This code, called PhysX², (to be presented in section II) will help to analyze the effects of chemistry in the coupled multi-physics phenomena.

B. Chemistry of fuel pyrolysis and of gas products combustion

The combustion is obtained by reaction of the gas products resulting from the solid fuel pyrolysis with the injected oxidizer. While the oxidizer mass flow rate is controlled, the production of gas species is not adjustable since it is due to heat and mass transfer inside the hybrid rocket. It depends on various physical and chemical phenomena (boundary layer thickness, mass flow rate, radiative heat flux, emissivity of the solid fuel). Due to the strong coupling which exists between pyrolysis and combustion, it is necessary to provide a fine analysis of chemical reactions that drive the entire process, thus the engine operation.

Generally, the solid fuels used in hybrid rockets are complex compounds such as polymers or heavy hydrocarbons chemical (Hydroxyl-Terminated PolyButadiene HTPB, Poly (Methyl MethAcrylate) PMMA, High Density Poly Ethylene HDPE and waxes). The reactions occurring in the chemical process of thermal degradation, ie. pyrolysis, depend on the nature of the solid fuel. Pyrolysis reactions break heavy species into smaller ones by thermal activation. Two pyrolysis mechanisms can be observed [13]: unzipping or random scission. Unzipping mechanism applies for the PMMA, i.e. the chemical process mainly produces the monomer molecule. This results in a relatively simple chemical mechanism. On the contrary, the random scission applies in the case of HDPE, i.e. the chemical process produces random lighter molecules of alkanes, alkenes and dienes. In this case, the chemical mechanism can be very complex involving thousands of species and reactions [14,15]. The pyrolysis process can continue in the gas phase. It is of first importance to consider all these species because the radicals (like CH_3 , see elementary reaction R. 1) play a major role in the diffusion and combustion processes.



As a consequence, the combustion mechanism also has to consider these species and highly detailed mechanism could be required to consider the related phenomena with fine analysis. Since the oxidizer and reducer flows are separated, a diffusion flame occurs where the reactant ratio is sufficient. Within the flame surface, very ephemera molecules, known as radicals (like OH, see elementary reaction R. 2), appear. The combustion mechanisms are numerous and are adapted to given couple oxidizer/reducer [16,17]. Those chemical mechanisms can be complex with tens to hundreds of species and hundreds to thousands of reactions.



C. Numerical simulations of hybrid engine

Compared to experimental studies on hybrid rocket, numerical studies present the great advantage to understand in details what happens in a combustion chamber. With the computational power increase of the last decade, more and more numerical studies on the operating of hybrid rocket engines have been published.

Cai and Tian [18] present several dedicated tools to investigate the fluid dynamics and the chemical process in order to mainly predict the engine performances. Serin and Gogus [19] propose a 1-D transient code with the regression rate model and a chemical equilibrium model for combustion. Another very recent Computational Fluid Dynamics (CFD) work is proposed by Stoia-Djeska and Mingireanu [20] with 1-D modeling to investigate the pressure oscillations and combustion instabilities. Kim and Kim [21] present a more sophisticated approach because they consider a Large Eddy Simulation approach for the turbulence and a soot formation model for a fine radiative transfer consideration. The lack of detailed chemistry consideration is the common point of all those codes. However, some of the authors indicate the importance of considering chemistry [18,19,22] with greater details than what was previously done.

Some authors have begun to overcome this lack of chemistry description. Rare codes simulating the hybrid rocket combustion chamber on transient state with a special chemistry consideration must be mentioned. Antoniou and Akyuzlu [23][24-26] solve the solid and fluid domains separately and then couple them through an interface consideration. The combustion is considered with a global reaction involving *only* three species with a kinetic scheme given by a single Arrhenius law. The regression rate is also determined by a global Arrhenius law and the energy absorption by pyrolysis is given by a latent heat factor [25]. A very similar work to this one has been conducted by Yang et al. [27]. In this later work, the chemistry is still not considered with better details. Those codes consider turbulence through a k-ε model, radiation heat transfer and the meshing is mobile to follow the shape deformation of the solid/gas phase interface during regression. Gariani et al. [28] proposed a turbulent gas phase modeled by a RANS approach, with a six-step combustion mechanism. Still, no radicals are considered and the flame structure could not be described with as details as it could be with a detailed chemical mechanism. The regression rate is computed by a global Arrhenius law as it is the case in the work of Antoniou and Akyuzlu and Yang et al.

In this context, the laboratory PRISME from the University of Orléans (France) is working since 2007 notably on the reducer pyrolysis to choose the best reducer/oxidizer couple depending on some selected criteria [29]. In

collaboration with CNES and Roxel, a PhD work began in 2009 on the study and the model of a hybrid combustion chamber. The numerical description of the phenomena inside the hybrid combustion chamber should be later validated by experimental data provided by a hybrid demonstrator test bench and a flash pyrolysis device coupled to gas chromatograph/mass spectrometer analysis. For now, a 2-D biphasic transient numerical code has been developed to focus on detailed chemistry. The feature of this new code and its validation are presented in this paper.

II. Development of the numerical code

In the hybrid rocket combustion chamber, the two main phases (solid fuel and gas flow) are considered with a biphasic approach. The presence of possible liquid phase or solid particles in gas flow is not considered. The physical behavior of the two main phases can be modelled by Partial Differential Equations (PDE). The two phases could have any shape on a Cartesian grid. Between them, the interface is considered with heat, mass and species transfer. The methodology used to solve those points is explained in the present section.

As a first approach, the code is simplified at physical description level. The turbulence is not considered and radiative heat transfer is simplified. Moreover, the numerical schemes applied are simple and limited to first and second orders. Due to large computation time expected, the code is developed in 2D. Those simplifications enable to focus on the development of the chemistry computation aspect.

A. Structure of the code

The code is written in Matlab language due to its ability to handle in a simple manner matrix element computation and due to its large amount of available functions and tools. The PDE are solved with the Finite Differences (FD) method on structured collocated grid with potentially non uniform spatial steps.

The Ordinary Differential Equation (ODE) solver Runge-Kutta 4-5 (RK45) algorithm is used to integrate the time derivatives of the PDE while the spatial derivatives are reconstructed as followed. Two schemes have been implemented.

The first one is the Central Difference Scheme (CDS) [30] which gives the first and second order derivatives by computing respectively the equations Eq. 1 and Eq. 2.

The second scheme is the first order Up-Wind Scheme (UWS) which is used for *convected* first order derivatives in order to stabilize the flow equations (Eq. 8 to Eq. 17). At the node i , if the flow goes forward, then the derivative take the value of the Backward Difference Scheme (BDS) computed by equation Eq. 3 (because it goes up to the stream or *upwind*). To the opposite, if the flow goes backward, then the derivative take the value of the Forward Difference Scheme (FDS) computed by equation Eq. 4. For derivatives along the y-axis the same methods are applied.

$$\left. \frac{\partial \phi}{\partial x} \right|_i = \frac{\phi_{i+1} - \phi_{i-1}}{x_{i+1} - x_{i-1}} \quad \text{Eq. 1}$$

$$\left. \frac{\partial^2 \phi}{\partial x^2} \right|_i = \frac{\frac{\phi_{i+1} - \phi_i}{x_{i+1} - x_i} - \frac{\phi_i - \phi_{i-1}}{x_i - x_{i-1}}}{\frac{1}{2}(x_{i+1} - x_{i-1})} \quad \text{Eq. 2}$$

$$\left. \frac{\partial \phi}{\partial x} \right|_i = \frac{\phi_i - \phi_{i-1}}{x_i - x_{i-1}} \quad \text{Eq. 3}$$

$$\left. \frac{\partial \phi}{\partial x} \right|_i = \frac{\phi_{i+1} - \phi_i}{x_{i+1} - x_i} \quad \text{Eq. 4}$$

The structure of the code, named PhysX2, is built to enable a step by step development and implementation of different functions and tools needed to run simulations. Therefore it enables step by step validations. Inside PhysX2, the data can be seen on three stages represented in Figure 1:

- The lowest layer contains the coordinates of each computations node (in black dots in the Figure 1). Since the data are collocated, at each computation node, other data are contained in upper layers.
- The second layer serves to define the different computational domains which can be considered. Sub-domains are defined by the set of nodes belonging to them respectively (red and blue filled dots for the sub-domain #1 and #2 respectively in the Figure 1). The red or blue empty dots show that the corresponding sub-domain is not present in the corresponding position in the computational grid.
- The upper layer stores all the variables (represented by green dots in the Figure 1) which are needed to solve the governing equations related to each domain. The Figure 1 illustrates that in the sub-domain #1 (in red) three variables (three stages of green dots) are solved (density, and velocity components for instance) while in the sub-domain #2 (in blue) one variable is solved (temperature for instance). One can note that the middle row of nodes belongs to both sub-domains. This location is the interface and it is governed by coupling boundary conditions.

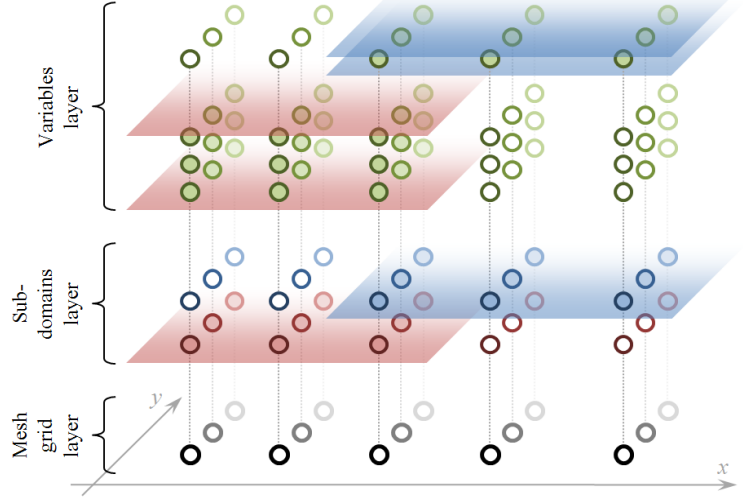


Figure 1: Multi layered data in PhysX2

B. Solid phase

The heat transfer within the solid fuel is computed by solving the heat equation Eq. 5. The heat fluxes corresponding to x and y-axis are denoted by q_x and q_y respectively. The source term p_{th} could be used to consider thermal power absorption by pyrolysis reactions and/or in deep radiation absorption of semi-transparent medium. However, the energy absorbed by pyrolysis reactions is taken into account by another way described further in section II.D. For now the source term related to heat absorption remains null.

$$\frac{\partial(T)}{\partial t} = \frac{-\frac{\partial(q_x)}{\partial x} - \frac{\partial(q_y)}{\partial y}}{\rho c} + \frac{p_{th}}{\rho c} \quad \text{Eq. 5}$$

With the heat fluxes computed by Eq. 6 and Eq. 7.

$$q_x = -\lambda \frac{\partial(T)}{\partial x} \quad \text{Eq. 6}$$

$$q_y = -\lambda \frac{\partial(T)}{\partial y} \quad \text{Eq. 7}$$

C. Gas Phase

C.1. Mass transfer

The variables are computed with the non-conservative forms. The equations Eq. 8 to Eq. 10 allow to model an isothermal and a chemically homogeneous gas. As mentioned in section II.A, the UWS (see Eq. 3 and Eq. 4) is used for convected derivatives (they are preceded by velocity variables). To ease the understanding of the following equations, the derivatives using UWS are marked with a star superscript. The next equations Eq. 8 to Eq. 19 are adapted from reference [31].

Continuity equation:

$$\frac{\partial(\rho)}{\partial t} = -v_x \frac{\partial^*(\rho)}{\partial x} - v_y \frac{\partial^*(\rho)}{\partial y} - \rho \left(\frac{\partial(v_x)}{\partial x} + \frac{\partial(v_y)}{\partial y} \right) \quad \text{Eq. 8}$$

Momentum equations:

$$\frac{\partial(v_x)}{\partial t} = -v_x \frac{\partial^*(v_x)}{\partial x} - v_y \frac{\partial^*(v_x)}{\partial y} + \frac{\frac{\partial(\tau_x - p)}{\partial x} + \frac{\partial(\tau_{xy})}{\partial y}}{\rho} + f_x \quad \text{Eq. 9}$$

$$\frac{\partial(v_y)}{\partial t} = -v_x \frac{\partial^*(v_y)}{\partial x} - v_y \frac{\partial^*(v_y)}{\partial y} + \frac{\frac{\partial(\tau_{xy})}{\partial x} + \frac{\partial(\tau_y - p)}{\partial y}}{\rho} + f_y \quad \text{Eq. 10}$$

Where τ_x , τ_y and τ_{xy} are the viscous stress tensor components computed by Eq. 11 to Eq. 13.

$$\tau_x = \frac{4}{3}\mu \frac{\partial v_x}{\partial x} - \frac{2}{3}\mu \frac{\partial v_y}{\partial y} \quad \text{Eq. 11}$$

$$\tau_y = \frac{4}{3}\mu \frac{\partial v_y}{\partial y} - \frac{2}{3}\mu \frac{\partial v_x}{\partial x} \quad \text{Eq. 12}$$

$$\tau_{xy} = \mu \left(\frac{\partial v_x}{\partial y} + \frac{\partial v_y}{\partial x} \right) \quad \text{Eq. 13}$$

C.2. Reacting flow equation

The species transport equation Eq. 14 has been implemented. It is applied on $N-I$ species [31], where N is the number of species considered in the combustion mechanism. The last species which is not computed is evaluated by subtracting one to the sum of the others species mass fractions. To minimize the relative error done by doing so, the specie evaluated that way is the major specie.

$$\frac{\partial(Y_i)}{\partial t} = -v_x \frac{\partial^*(Y_i)}{\partial x} - v_y \frac{\partial^*(Y_i)}{\partial y} - \frac{\frac{\partial(j_{xi})}{\partial x} + \frac{\partial(j_{yi})}{\partial y}}{\rho} + \frac{\dot{\omega}_i}{\rho} \quad \text{Eq. 14}$$

Where j_{xi} and j_{yi} are the diffusion flux components computed by Eq. 15 and Eq. 16, and ω_i is the net production rate of the i^{th} specie.

$$j_{xi} = -D_{mi} \frac{\partial(Y_i)}{\partial x} \quad \text{Eq. 15}$$

$$j_{yi} = -D_{mi} \frac{\partial(Y_i)}{\partial y} \quad \text{Eq. 16}$$

C.3. Heat transfer

For a non isothermal fluid, convective and conductive heat transfers must be considered. The temperature is computed by the equation Eq. 17 (assuming that c_v is constant during the integration step):

$$\begin{aligned} \frac{\partial(T)}{\partial t} = \frac{1}{c_v} & \left[-v_x \frac{\partial^*(u)}{\partial x} - v_y \frac{\partial^*(u)}{\partial y} + f_x \sum_{i=1}^N j_{xi} + f_y \sum_{i=1}^N j_{yi} \right. \\ & \left. + \frac{-\frac{\partial(q_x)}{\partial x} - \frac{\partial(q_y)}{\partial y} + (\tau_x - p) \frac{\partial(v_x)}{\partial x} + (\tau_y - p) \frac{\partial(v_y)}{\partial y} + \tau_{xy} \left(\frac{\partial(v_x)}{\partial y} + \frac{\partial(v_y)}{\partial x} \right)}{\rho} \right] + \frac{p_{th}}{\rho c_v} \end{aligned} \quad \text{Eq. 17}$$

Where q_x and q_y are the thermal flux components (which take into account conduction and interdiffusion) computed by Eq. 18 and Eq. 19, and p_{th} is the thermal power source term.

$$q_x = -\lambda \frac{\partial(T)}{\partial x} + \rho T \sum_{i=1}^N c_{pi} j_{xi} \quad \text{Eq. 18}$$

$$q_y = -\lambda \frac{\partial(T)}{\partial y} + \rho T \sum_{i=1}^N c_{pi} j_{yi} \quad \text{Eq. 19}$$

C.4. Fluid properties

The equation system is closed by the perfect gas law state equation Eq. 20:

$$p = \rho \mathcal{R} T \sum_{i=1}^N \frac{Y_i}{Mw_i} \quad \text{Eq. 20}$$

The solver Cantera [32] is used to compute mixture properties: viscosity, mixture diffusive coefficient and conductivity. These properties are required to compute respectively the terms τ_x , τ_y and τ_{xy} , j_{xi} and j_{yi} , and q_x and q_y which appeared in the previous equations Eq. 8 to Eq. 14, Eq. 14 and Eq. 17.

In the equations Eq. 14 and Eq. 17 the source terms ω_i and p_{th} could refer to the net production rate and the net power thermal density respectively, generated by the chemical reactions. These terms are considered outside the equations thanks to a variable splitting method presented in the following section II.D. The RK45 algorithm is not suited for integrating chemistry because reactions are too stiff.

D. Chemistry

The solver Cantera [32] is used to compute the mass fractions and temperature of both gas and solid phases. For a given chemical mechanism, it solves temperature and species mass fractions thanks to equations Eq. 21 and Eq. 22 respectively.

$$\frac{d(\rho u)}{dt} = - \sum_{i=1}^N \dot{\omega}_i \Delta h_{f_i}^0 \quad \text{Eq. 21}$$

$$\frac{d(Y_i)}{dt} = \frac{\dot{\omega}_i}{\rho} \quad \text{Eq. 22}$$

The mass rate of production ω_i of i^{th} specie is computed by equation Eq. 23 [31] in which the reaction rate R_k of the k^{th} reaction is computed by the modified form of the Arrhenius law (see Eq. 24). The numbers N and M are the number of species and reactions respectively of the given chemical mechanism.

$$\dot{\omega}_i = Mw_i \sum_{k=1}^M (v''_{i,k} - v'_{i,k}) B_k T^{\alpha_k} \exp\left(-\frac{E_{ak}}{RT}\right) \prod_{j=1}^N \left(\rho \frac{Y_j}{Mw_j}\right)^{v'_{j,k}} \quad \text{Eq. 23}$$

$$R_k = B_k T^{\alpha_k} \exp\left(-\frac{E_{ak}}{RT}\right) \quad \text{Eq. 24}$$

These equations correspond to a 0-D description. They are applied to each node, assuming that during the time step Δt of the solver, they can be considered as a set of independent 0-D chemical reactor. This hypothesis is acceptable under certain conditions, notably on flow velocity. This point is validated in section III.C.

Figure 2 shows how the RK45 solver converges when error *err* meets the tolerance *tol*. By coupling the stiff chemistry with the physics in the same RK45 algorithm, the integration time step Δt could be refined indefinitely because of the difficulty to converge. As a result chemistry and physics must be decoupled. Figure 2 shows that the solution y^{n+1} of the $n+1^{\text{th}}$ iteration is overwritten, following the blue path, to y^{*n+1} taking into account the chemistry computation.

This strategy corresponds to the superposition principle. It assumes that during one iteration time step, the physical evolution is weakly dependent on the chemistry evolution and vice versa. This process is illustrated for one node in the Figure 3 in black dashed arrows, while the *real* solution along the time step is the red arrow. The RK45 solver computed a solution y^{n+1} at t^{n+1} from the previous solution y^n at t^n . To account for the chemistry evolution, the state y^{n+1} is taken as the starting point of the chemistry computation which returns a new state noted y^{*n+1} at t^{n+1} after computing a Δt time step. The new state y^{*n+1} computed is assumed to be the actual solution of the coupled problem. The assumption made by decoupling physic and chemistry, may generate errors on state and time (respectively noted y_{error} and t_{error}) which have been evaluated in section III.C.

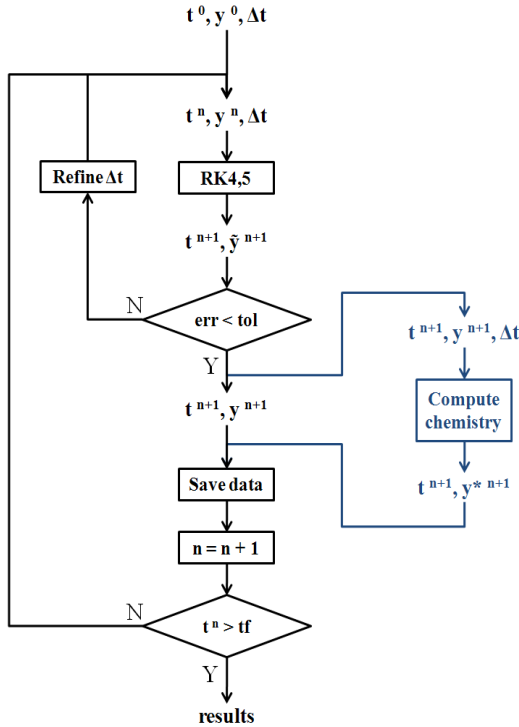


Figure 2: Modifications (in blue) of the original RK45 algorithm

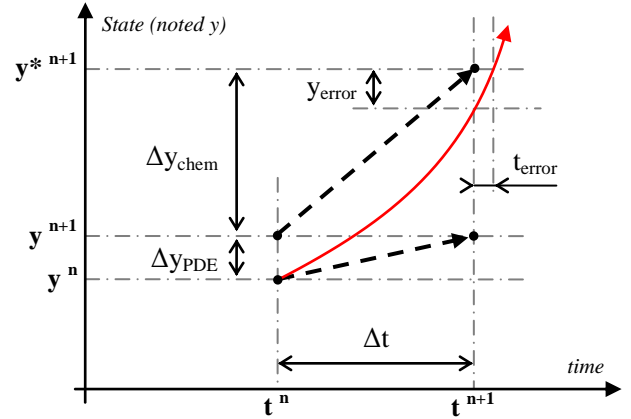


Figure 3: Superposition principle variables overview

III. Validation of the code

The numerical code has been validated through comparisons to analytical and numerical test cases. Before considering hybrid engine, academic cases were considered to validate the governing equations.

A. Solid phase

The first case is the transient heat conduction in semi-infinite 1-D material. The extremity of the medium at $x = 0$ is set at T_0 . The initial and boundary conditions are expressed by:

$$\begin{cases} T(x > 0, t = 0) = T_\infty \\ T(x = 0, t) = T_0 \end{cases}$$

The analytical solution of the problem is given by the equation Eq. 25 [33]. The code takes a finite material into account and the numerical domain can be considered as infinite only at the early stage of the calculation, until the heat transfer reaches the other extremity of the simulated domain. The thermodynamic properties of the medium, the polyethylene, are constant and uniform and given in Table 1.

$$T(x, t) = T_0 + (T_\infty - T_0) \operatorname{erf} \left(\frac{x}{2\sqrt{t}} \sqrt{\frac{\rho c}{\lambda}} \right) \quad \text{Eq. 25}$$

Table 1: Numerical values used for the validation case

	Symbols	Values
Heat conductivity	λ	0,48 W.m ⁻¹ .K ⁻¹
Density	ρ	950 kg.m ⁻³
Heat capacity	c	2200 J.kg ⁻¹ .K ⁻¹
Initial temperature	T_∞	500 K
Boundary temperature	T_0	300 K

Figure 4 shows the temperature profile within the solid at various instants. Until $t = 50$ minutes, the temperature profile meets the analytical solution quite accurately. After that, the numerical solution tends to the steady state with a linear temperature profile between the left and right extremities of the domains held at T_0 and T_∞ respectively. While the semi-infinite medium is a valid assumption, the accuracy of the results are more than 99,9% for all nodes. The disagreement with analytical solution shown at 200 minutes shows that the semi infinite medium assumption is not valid any longer. The right boundary condition does not match with this assumption.

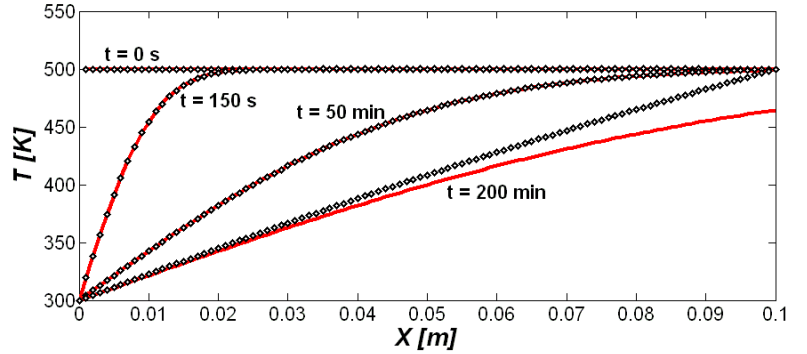


Figure 4: Transient states at various instants of temperature profile along the x-axis matching the analytical solutions while semi infinite medium hypothesis is valid (— analytical solutions, \diamond numerical solutions)

The second case validates the implementation of space varying thermodynamic properties into the heat equation. A pile of two different materials with an ideal contact (no temperature discontinuity in the interface) is considered, under a temperature gradient. The initial and boundary conditions are expressed by:

$$\begin{cases} T(x, t = 0) = T_c + x \frac{T_h - T_c}{e} \\ T(x = 0, t) = T_c \\ T(x = l, t) = T_h \end{cases}$$

The analytical solution of the steady state is given by the set of equations Eq. 26 where ϕ is the heat flux at steady state passing through materials. The two materials considered are polyethylene (noted PE) and polystyrene (noted PS) as an example. Their thermodynamic properties are reported in the Table 2 among the other parameters used in the simulation.

$$\begin{cases} T(x < l/2) = T_c + \frac{\phi}{\lambda_{PE}} x \\ T(x > l/2) = T_h + \frac{\phi}{\lambda_{PS}} (x - l) \end{cases} \quad \text{Eq. 26}$$

Table 2: Numerical values used for the validation case

	Symbols	Values	
Heat conductivity	$\lambda_{PE} \lambda_{PS}$	0,48 W.m ⁻¹ .K ⁻¹	0,12 W.m ⁻¹ .K ⁻¹
Density	$\rho_{PE} \rho_{PS}$	950 kg.m ⁻³	1040 kg.m ⁻³
Heat capacity	$c_{PE} c_{PS}$	2200 J.kg ⁻¹ .K ⁻¹	1360 J.kg ⁻¹ .K ⁻¹
Boundary temperatures	$T_c T_h$	300 K	500 K
Domain thickness	l	0,1 m	

A unique material with varying properties, on one sub-domain, can be considered or two sub-domains, each with constant properties of PE and PS, could be preferred. For this later possibility, boundaries conditions must be applied to *link* the two sub-domains. The boundary conditions at the interface of the two sub-domains must be related to temperature and heat flux continuity, therefore, the first condition is a Dirichlet condition (the interface temperature of the sub-domain #1 is imposed with the one of the sub-domain #2), and the second one is a Neumann condition (the interface heat flux of the sub-domain #2 is imposed with the one of the sub-domain #1). The boundary conditions can be reversed without impacting the results.

$$\begin{cases} T_{\#1}(x = l/2) = T_{\#2}(x = l/2) \\ \lambda_{PS} \left(\frac{\partial T_{\#2}}{\partial x} \right) (x = l/2) = \lambda_{PE} \left(\frac{\partial T_{\#1}}{\partial x} \right) (x = l/2) \end{cases}$$

The temperature profile of the steady state is presented in Figure 5. The results obtained with the boundary conditions as expressed above are represented by right pointing triangles. The revert boundary conditions are represented by left pointing triangles (which appear hidden by the right pointing triangles due to very close results). The analytical solution is represented by a solid line that is superimposed on numerical results. The simulation taking into account one sub-domain with a discontinuity of spatial thermodynamic properties is represented by diamonds in Figure 5. The enlarged figure shows that the diamonds' line does not match perfectly the analytical solution which is caused by the thermodynamic properties discontinuity between two nodes. However, the relative error at the interface is about 0,15% which can be considered acceptable in that case. Moreover, this error is expected to be lowered with a finer grid. With a two sub-domains simulation (marked by triangles in Figure 5), the accuracy is very good (less than 1×10^{-6} K in absolute temperature error).

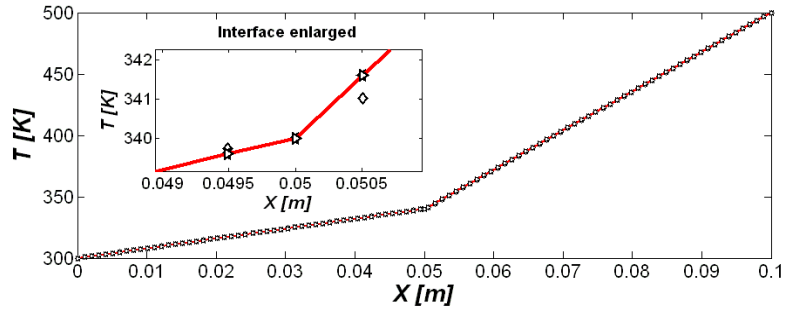


Figure 5: Temperature profile at steady state of a sandwich material (— analytical solution, \diamond one sub-domain simulation solution, \triangleleft and \triangleright two sub-domains simulation solutions)

These two validation cases have been done on 1-D description along the x-axis. Same results are obtained on the y-axis.

B. Gas phase

The first validation cases focus on the continuity and momentum equations (section B.1). The temperature equation (section B.2) and the multi-species transport equation (section B.3) have been also considered in the last cases.

B.1. Fluid flow validation

Four cases are presented to validate the Navier-Stokes equations. The first one aims at studying the establishment length of the boundary layer in a constant area finite channel at steady state configuration. The parameters used for this simulation are given in Table 3. The inlet velocity has a flat cross sectional profile. It is expected at the outlet that the horizontal velocity component tends to parabolic cross sectional profile. Horizontal velocities have been compared to results obtained with Fluent software (made by Ansys) for different longitudinal positions. The model used in Fluent is laminar model with near wall mesh refined (see Figure 7). The simulation on PhysX² has been done with non constant spatial step mesh (see Figure 6). The comparison is presented in Figure 8 and shows a good agreement.

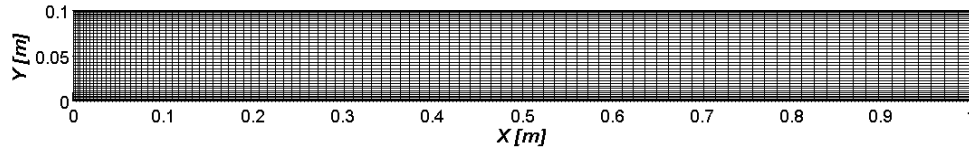


Figure 6: Near wall and near entrance refined mesh (101×41)

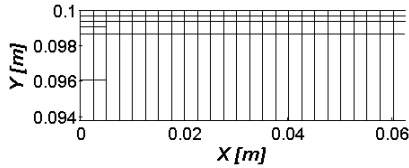


Figure 7: Up right corner mesh of Fluent simulation

Table 3: Numerical values used for the validation case

	Symbols	Values
Length	L	1 m
Height	H	0,1 m
Velocity inlet	u_{in}	10 m.s ⁻¹
Density inlet	ρ_{in}	1 kg.m ⁻³
Viscosity	μ	1.10 ⁻³ Pa.s

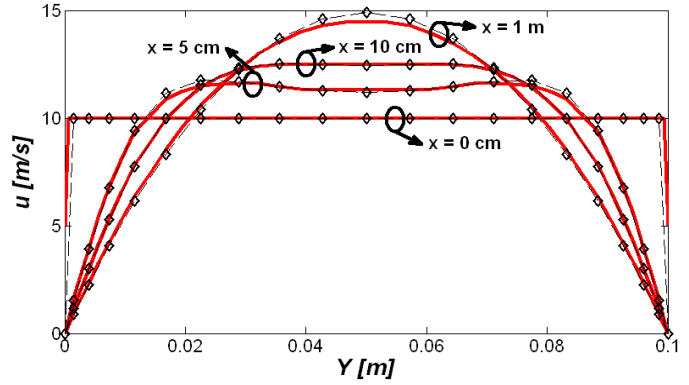


Figure 8: Cross sectional horizontal velocity along the channel at steady state (— Fluent solutions, \diamond current code solutions)

The second case aims at studying the boundary layer thickness over a flat plate in a free stream at steady state. The parameters used for this simulation are given in Table 4. The inlet velocity has a flat cross sectional profile and it is purely horizontal. It is expected to have a boundary layer development along the length of the flat plate. The Blasius solution provides the analytical form (Eq. 27) of the boundary layer thickness $\delta_{95\%}$ at 95% of the main stream flow velocity [34].

Table 4: Numerical values used for the validation case

	Symbols	Values
Length	L	1 m
Velocity inlet	u_{in}	50 m.s ⁻¹
Density inlet	ρ_{in}	1 kg.m ⁻³
Viscosity	μ	1.10 ⁻⁴ Pa.s

$$\frac{\delta_{95\%}}{x} = 3,878 \times Re_x^{-0.5}$$

Eq. 27

The numerical solution versus the analytical one is presented in Figure 9. A good general agreement is found. The meshing along the x-axis has been refined at the inlet to accurately describe the development of the boundary layer. However the relative error found at the inlet is higher than in the rest of the flow. From $x = 0,2$ cm to the end of the simulated domain, the relative error varies from -0,2% to 0,5%.

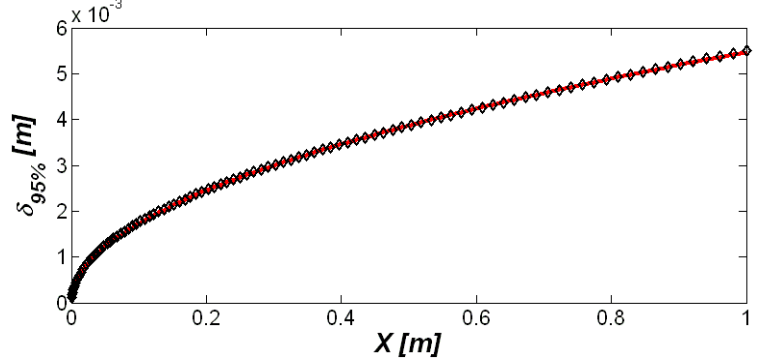


Figure 9: Dynamic boundary layer profile at steady state (— analytical solution, \diamond current code solutions)

The third case corresponds to a flow behind a descending step at steady state in order to validate the recirculation flow pattern. A flat cross sectional inlet velocity is used to generate the flow. The step is placed at 10 cm after the inlet and its height is 7 cm. The total length of the domain is 60 cm to let the expected vortex behind the step to be fully developed. All the parameters of this simulation are given in Table 5.

Table 5: Numerical values used for the validation

	case	
	Symbols	Values
Length	L	0,6 m
Height	H	0,2 m
Step length	L_{step}	0,1 m
Step height	H_{step}	0,07 m
Velocity inlet	u_{in}	10 m.s ⁻¹
Density inlet	ρ_{in}	1 kg.m ⁻³
Viscosity	μ	6,5.10 ⁻³ Pa.s

The reference case has been running on Fluent using a laminar model, (since PhysX² does not implement any turbulence model). In order to reproduce the flow field obtained with a k- ϵ turbulence model and an associated viscosity of 2×10^{-5} Pa.s with a laminar model, the viscosity has been increased till $6,5 \times 10^{-3}$ Pa.s. The comparison that is performed in Figure 10 is between the Fluent laminar computation with this new viscosity value and the PhysX² computation with the same viscosity value. It shows the streamlines over the flow field. The white streamlines represent the frontier of the vortex. Any particle exterior to those lines should returns to the main flow. A qualitatively good agreement is found. Figure 11 compares the velocity

components in section at $y = 0,04$ cm passing by the vortex center. The vertical velocity component shows a quantitatively good agreement while a slight difference remains for the horizontal velocity. Hence the vortex centers are not at the exact same location. The vortex centers are determined by finding the smallest stream-lines. The reference case gives the vortex center at the coordinates ($x = 0,2086$ m and $y = 0,0399$ m) and the PhysX² code gives the vortex center at the coordinates ($x = 0,2066$ m and $y = 0,0405$ m). This result has been achieved with mesh at constant step size for PhysX², while Fluent used a near wall refined mesh.

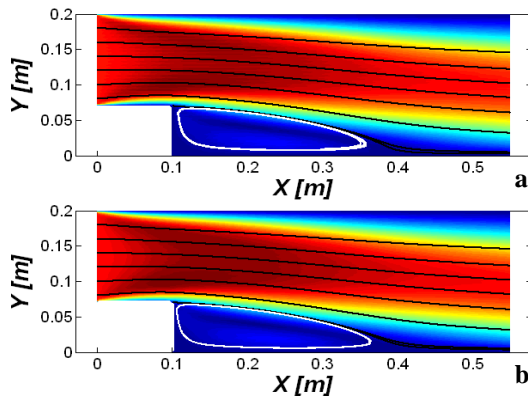


Figure 10: Vortex shape and boundaries at steady state on PhysX² (a) and Fluent (b)

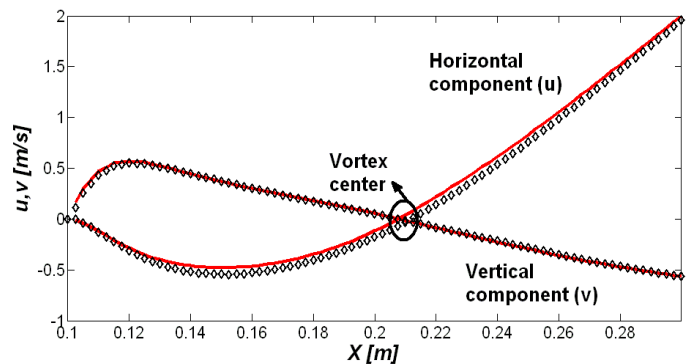


Figure 11: Velocity components in section passing by vortex center at steady state (— Fluent solutions, \diamond current code solutions)

A last validation case on isothermal viscous fluid has been conducted, which aims at simulating a driven cavity flow. This case has been studied for various Reynolds number by Ghia et al. [35] and those cases have served as validation cases in the PhD work of Antoniou [23]. It has been decided to use those as well. The case with Reynolds number of 100 has been run and compared to Ghia et al. results. The conditions used for simulation are illustrated in Figure 12 and reported in Table 6. Figure 13.a shows the horizontal velocity component along the vertical median section (passing by the cavity center point). Figure 13.b shows the vertical velocity component along the horizontal median section. The results are obtained at steady state. The case show good agreement with the Ghia et al. results, with a maximum relative error of 4% at the minimum vertical velocity point.

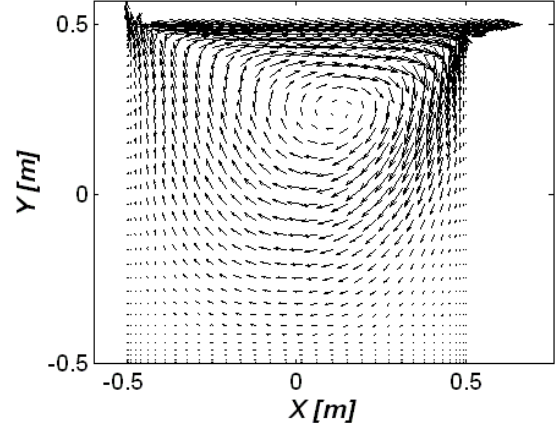


Figure 12: Velocity flow field in the driven cavity

Table 6: Numerical values used for the validation cases

	Symbols	Values
Reynolds	Re	100
Length	L	1 m
Height	H	1 m
Mean density	ρ	1 kg.m ⁻³
Shear velocity	u_{shear}	1 m.s ⁻¹
Viscosity	μ	10.10 ⁻³ Pa.s

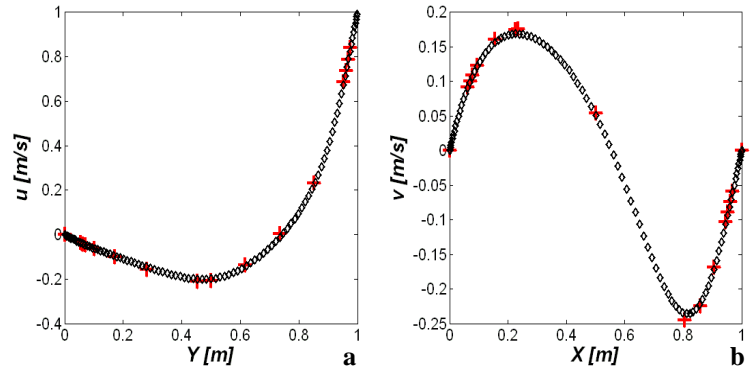


Figure 13: Good agreement at steady state on horizontal (a) and vertical (b) velocity components of the two CFD results (+ Ghia et al. solutions, \diamond current code solutions)

B.2. Non isothermal flows

With the energy balance equation (Eq. 17) coupled to the Navier-Stokes equations (Eq. 8, Eq. 9 and Eq. 10), shocks can be simulated. Sod [36] was chosen as reference work, because he tested many schemes and their respective results on simulating 1-D shock wave propagation are shown. In the Sod problem, a frontier at x_0 separates two regions held at different densities and pressures. At $t = 0$, the shock between the two regions is propagating into the medium. The parameters used by Sod and for the validation case are summarized in Table 7.

Table 7: Numerical values used for the validation case

	Symbols	Values
Densities	$\rho_{left} \rho_{right}$	1 kg.m ⁻³ 0,125 kg.m ⁻³
Velocities	$v_{left} v_{right}$	0 m.s ⁻¹ 0 m.s ⁻¹
Pressures	$p_{left} p_{right}$	1 Pa 0,1 Pa
Specific heats ratio	γ	1,4
Frontier position	x_0	0,5 m

Figure 14 shows the PhysX2 flow variable profiles in the shock tube superposed to the analytical profiles. The fronts of density and energy between zones III and IV appeared hardly smoothed due to the first order scheme while the shock (between zones IV and V) is quite stiff for all variables with oscillations due to the second order centered scheme after the shock. The shock is also delayed compared to the analytical solution. Moreover, the energy level within the zone IV is badly accurate (5% of relative error) while other variables are at least 98% accurate. In the zones I to III, all variables show fair accuracy. The same case has been run along the y-axis with similar results.

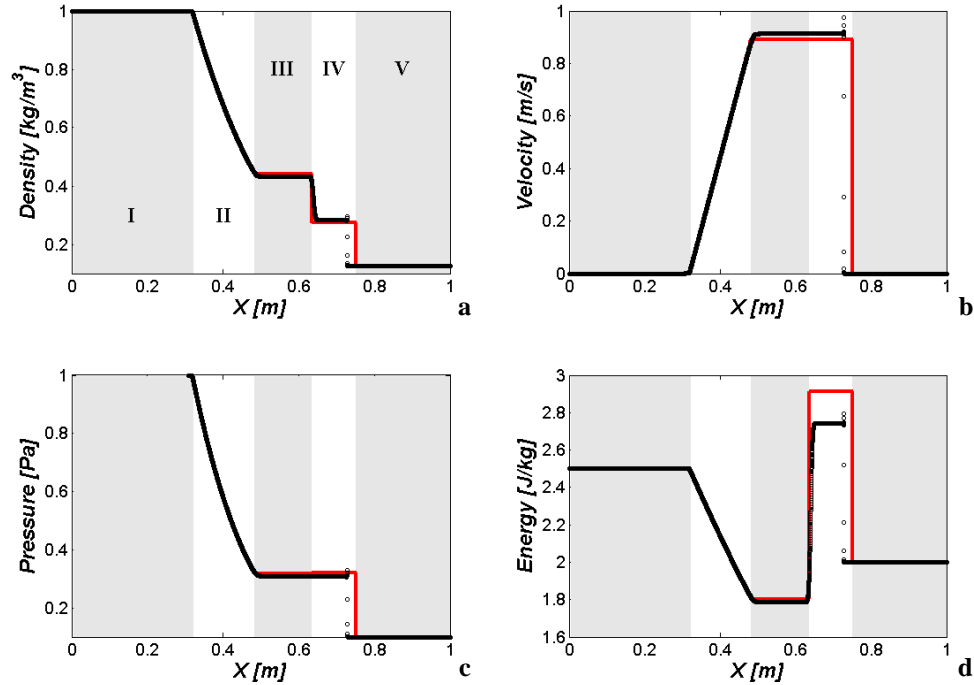


Figure 14: Profile of density (a), velocity (b), pressure (c) and internal energy (d) for the Sod's shock problem along the x-axis at the instant $t = 0,153$ s (— analytical solutions, ○ numerical solutions)

The mass and energy conservation has been validated on a second test case with a gas enclosed in an adiabatic box. At initial state, a hot zone is held in the bottom left quarter of the box. To have an initial uniform pressure, the density of the gas is set accordingly. With a gravity field, a natural convective heat and mass transport are established. Figure 15 illustrates at some various instants the temperature field. The mass and energy conservation are computed respectively by Eq. 28 and Eq. 29 where t_z refers to the thickness (in the z-axis direction) of the domain simulated.

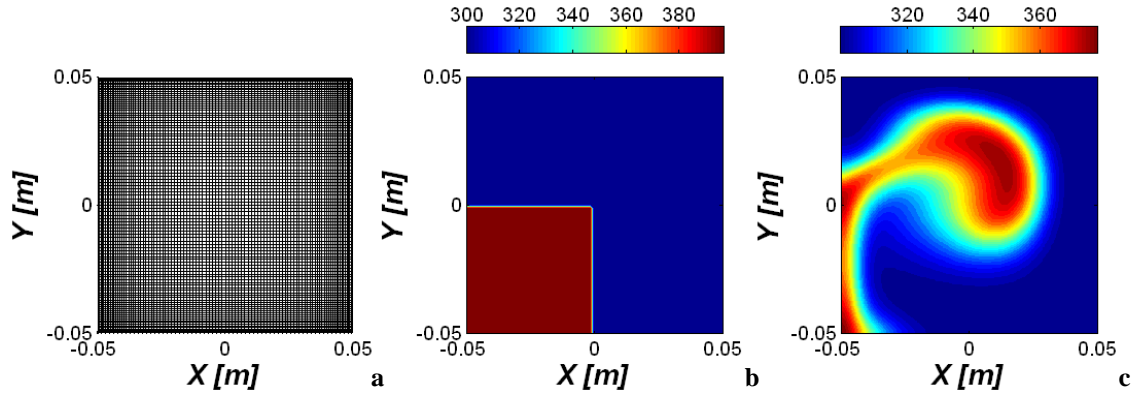


Figure 15: Near wall refined mesh with 101×101 nodes (a) initial condition for temperature (b) and natural convection of temperature at $t = 0,2$ s (c)

$$\frac{m(t)}{t_z} = \iint_{\mathcal{D}} \rho(t) \cdot dS \quad \text{Eq. 28}$$

$$\frac{e(t)}{t_z} = \iint_{\mathcal{D}} \rho(t) \left(c_v T(t) + \frac{v(t)_x^2 + v(t)_y^2}{2} + y f_y(t) \right) \cdot dS \quad \text{Eq. 29}$$

A first run has been done on a wall refined meshing of 101×101 nodes. Figure 16 shows the mass and energy conservation discrepancies which tend to around 0,3% for both. By dividing by a factor two the density of nodes in each direction (i.e. in a 51×51 nodes meshing) the mass and energy conservation error increases to around 0,6%. A criterion should be fixed on the energy and mass conservation to define the coarsest grid which can be used with the right equilibrium between accuracy and computation cost. For this current case, dividing by two the number of nodes in each direction increase the error on mass conservation by 1,8 and energy conservation by 1,6. It also decreases by a factor of 5 the time computation.

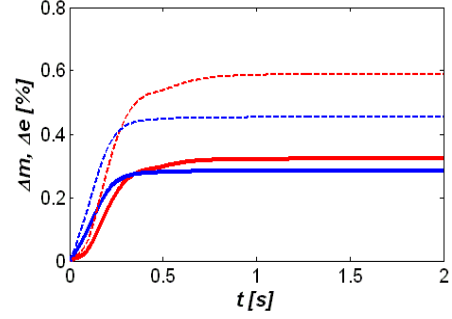


Figure 16: Mass (in red) and energy (in blue) conservation error with a 101x101 nodes grid (in solid bold lines) and coarse 51x51 nodes grid (in dashed lines)

B.3. Multi-species flow

Finally the multi-species transport equation Eq. 14 has been validated. The sum of all mass fractions which should be equal to one has been verified by exceptionally computing the transport equation for all species (instead of computing it for all minus one to balance the error in the major compound).

Two gases initially separated by a membrane in a tube are considered. At $t = 0$, the membrane is removed to let the gases diffusing in each other. It is expected that at steady state the mixture becomes uniform. In this validation case, the convective transport is disabled, hence the velocity components remain constant at zero. Figure 17 shows the evolution between initial to final state of the mass fractions profile for both species. Since at initial state, there is 75% of the first specie (in red) and 25% of the second one, it is verified that the final mixture conserves those proportions. Moreover, at anytime and anywhere during the simulation, the difference between the sum of mass fraction and 1 is below 1×10^{-6} which is the relative tolerance given to the solver.

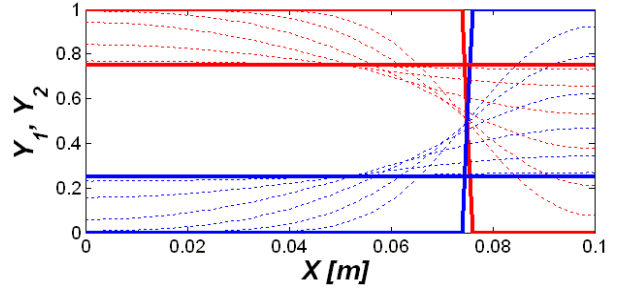


Figure 17: Mass fractions conservation at various instants (the first specie in red and the second in blue), initial and steady state are in solid lines

Since this latest validation case is a 1-D problem oriented along the x-axis, and in order to validate the behavior on the other direction, the same case was run along the y-axis. The very same results have been obtained.

C. Chemistry

Since chemistry is not fully coupled with physical phenomena by applying the superposition principle, the impact on this procedure must be studied in order to determine at which extent this principle is suitable. The *physical* parts of the generic equations Eq. 30 and Eq. 31 can be simulated by heat and species sources. Four validation cases, using the Grimech3.0 [16] as detailed chemical mechanism (53 species and 325 reactions), were performed to study the influence of the superposition principle on the combustion of ethylene/oxygen mixture in various conditions given in Table 8. 0-D fully coupled simulations (without splitting the physical and chemical variables) are also solved to serve as reference test cases.

$$\frac{d(\rho u)}{dt} = \frac{d(\rho u)}{dt}_{\text{physical}} + \frac{d(\rho u)}{dt}_{\text{chemical}} \quad \text{Eq. 30}$$

$$\frac{d(Y_i)}{dt} = \frac{d(Y_i)}{dt}_{\text{physical}} + \frac{d(Y_i)}{dt}_{\text{chemical}} \quad \text{Eq. 31}$$

Table 8: Numerical values used for the validation cases

Symbols	Values
---------	--------

Case number		#1	#2	#3	#4
Initial conditions	T	298 K			
	p	1 atm			
	X_{O_2}	0,75	0,75	1	0
	$X_{C_2H_4}$	0,25	0,25	0	1
	X_{Ar}	0	0	0	0
Rates	p_{th}	1 GW.m ⁻³			
	ω_{O_2}	0	0	300 s ⁻¹	0
	$\omega_{C_2H_4}$	0	0	0	50 s ⁻¹
	ω_{Ar}	0	200 s ⁻¹	0	0

In the case number #1, an initial stoichiometric mixture at standard conditions is observed the effect of each term in Eq. 30 and Eq. 31. In the cases #2 to #4 the mass fractions variations observed in Figure 18 before ignition are due to that species are added into the system, i.e. the sum of mass fractions remains equal to one. For instance, the case #4 starts with an initial composition of 100% of reducer, while oxidizer is added over the time span of the simulation. That is why in Figure 18.a the red curve shows an increase of oxidizer mass fraction while the reducer mass fraction is decreasing in Figure 18.b.

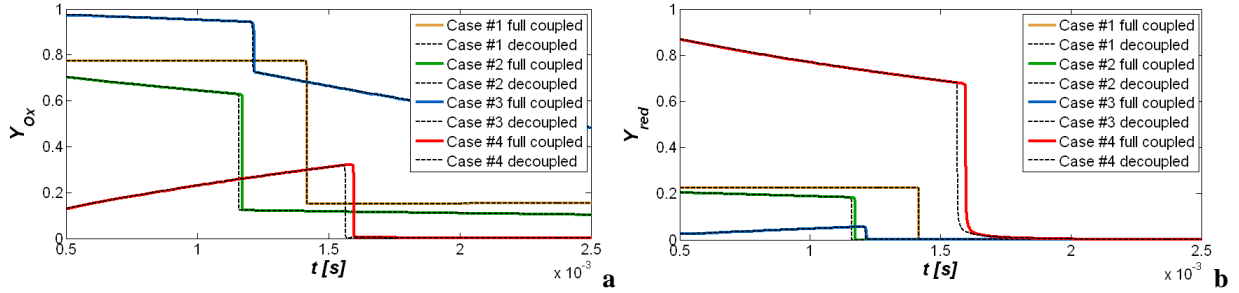


Figure 18: Oxidizer (a) and reducer (b) mass fractions evolution

Figure 19 shows the temperature time evolution of the four validation cases. In solid colored lines the full coupled solutions are represented and in black dashed lines the decoupled solutions. Before and after ignition, for those four validation cases, the results of the decoupled resolution are fairly accurate. At the ignition, there are time shifts for each case, varying from 1μs for the case #1 to 30 μs for the case #3. Relatively with the ignition delay, it represents a relative error from 0,1% to less than 2%. The error made on the ignition delay by decoupling the physical and the chemical phenomena is acceptable. Depending on the flow velocity, this error will impact the flame height above the solid fuel and thus the heat transfer. Discussions of the future results will focus on this aspect.

Further investigations have shown the lack of influence of the time step Δt chosen by the solver. The decoupled simulations shown in Figure 19 have been done with a forced time step of 10 ns in order to have a good resolution at the ignition. With larger time step (up to 10μs), the results are very similar (but do not described the ignition front).

Moreover, the error committed on the ignition delay follows a linear rule with respect to the rate at which species are put into the system (see the cases 5 to 8 in Table 9). With further investigations, an estimator of the ignition delay error committed by decoupled simulations has been build. Table 9 synthesized the other conditions studied to build the error estimator Eq. 32 and represented in Figure 20.

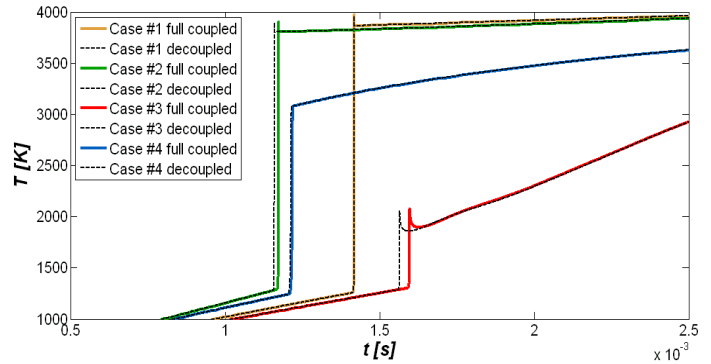


Figure 19: Differences on ignition delay in various conditions with full coupled simulation and split resolutions

$$err = \left(-7,4 \times \frac{\sum \omega_i}{p_{th}^{0.87}} + 45 \right) \times 10^{-3} \quad \text{Eq. 32}$$

Where *err* is the delay ignition error committed expressed in %, $\sum \omega_i$ is the sum of all specie source terms expressed in s^{-1} and p_{th} is the heat source expressed in $GW.m^{-3}$ (or $1 \times 10^9 W.m^{-3}$).

This estimator could serve as an indicator of results accuracy for hybrid combustion chamber simulations. Nevertheless this estimator must be taken with precautions, it has been built with a fixed range of values for p_{th} and $\sum \omega_i$, consequently it might be unreliable outside this range of values. The cases which have led to this estimator, have been run with the Grimech3.0 [16] chemical mechanism, therefore it should not be applied for other chemical mechanism. This specific point is mainly given as illustrative purpose. It shows that in future simulations, it will be possible to estimate the error done on the ignition delay for any combustion mechanism that will be used.

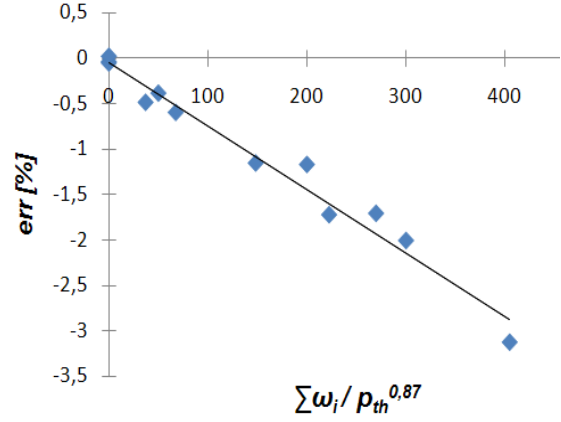


Figure 20: Linear estimator of the error on ignition delay

Table 9: Delay ignition relative errors in various conditions

	$p_{th} [GW.m^{-3}]$	$\sum \omega_i [s^{-1}]$	$err [\%]$		$p_{th} [GW.m^{-3}]$	$\sum \omega_i [s^{-1}]$	$err [\%]$
1	0,1	0	-0,04	7	1	300	-2,01
2	0,1	20	-1,15	8	1	50	-0,38
3	0,1	30	-1,72	9	10	0	0,02
4	0,1	5	-0,45	10	10	2000	-1,71
5	1	0	-0,05	11	10	3000	-3,13
6	1	200	-1,17	12	10	500	-0,59

IV. Conclusions and perspectives

Among the available technologies giving access to space, such as liquid and solid propellant rockets, hybrid rocket is emerging in the framework of civilian applications for safety, simplicity and cost reasons. Numerous studies and patents are related to hybrid propulsion and the research activities are found in the US, Europe and Asia. They are generally focusing on the development of solid fuel with high regression rate, on the oxidizer injection and on the system conception. Experiments are found with reduced and full scale test rigs and some numerical codes do exist. Nevertheless, hybrid rocket studies still suffer from a lack of consideration for the chemical phenomena which drive the overall phenomena in hybrid rocket. Indeed, the solid reducer pyrolysis generates the fuel and, depending on the chemical species to be generated, the ignition delay will vary (and consequently the distance of flame to solid surface, the heat flux applied to the solid surface and thus the regression rate). The chemical induction delay of pyrolysis also plays a role on the longitudinal position of the diffusion flame. Numerical simulation is the easiest way to investigate the chemistry effect and no code to the author's knowledge considers detailed chemical mechanism for solid fuel pyrolysis and for the combustion of pyrolysis products with the oxidizer.

A 2-D compressible reactive transient numerical code has been developed by the University of Orléans (France), in collaboration with the company Roxel and CNES. The solid and gas phases are described. The code takes the detailed chemistry into account (about a thousand species and ten thousands reactions). The governing phenomena equations have been given in this paper and the main validation test cases have been presented. The heat transfer within the solid fuel was validated for both transient and steady state and compared to analytical solutions. The continuity and momentum equations have been validated at steady state on the dynamic boundary layer thickness and its establishment length compared to analytical solutions. It has been also validated on recirculation flow behind a step compared with the same case simulated with Fluent CFD software and in cavity driven case compared to reference CFD results. An analytical solution of shock wave propagation has been used to validate the flow dynamic in transient state. Mass and energy are conserved with a suitable grid. Nevertheless, allowing slight discrepancies on conservation decrease the density of the meshing and increase the computation speed. Species

conservation has been verified in both steady and transient states. For chemistry consideration, the superposition principle is applied. 0-D validation cases have validated the applicability of the principle.

The source term in energy equation in solid phase should now be detailed to model heat absorption. Further validations should be conducted by comparison to other computational codes on full scale reacting flow case. The grid size should be defined depending on the accuracy required on mass and energy conservation. The time step used to decouple physical and chemical phenomena should be now indexed on the accuracy which is expected because it impacts the ignition delay and thus the flame position in the combustion chamber. Experimental data should be used to definitely determine the accuracy and the ability of the code. A test bench in Roxel company (Bourges) is currently under manufacturing and installation.

Due to computation time issues inherent to detailed chemistry, computation strategies are being developed. The code will now be intensively used to investigate the chemical process in hybrid combustion chamber. Using detailed chemistry for hybrid rocket combustion chamber is the originality of the numerical code. The results to be waited should provide highly valuable data to enhance the scientific and technologic understanding of hybrid rockets. This work will be supported by experiments to be performed in the second half of 2011.

Acknowledgments

This work is supported by the French national space agency CNES and by the company Roxel in the framework of the PERSEUS program. The authors wish to thank every person who is involved in this work and who is supporting it.

References

- [1] M.J. Chiaverini and K.K. Kuo, eds., *Fundamentals of Hybrid Rocket Combustion and Propulsion*, American Institute of Aeronautics and Astronautics, Inc., 2006.
- [2] W.H. Knuth, M.J. Chiaverini, D.J. Gramer, and J.A. Sauer, "Solid-Fuel Regression Rate Behavior of Vortex Hybrid Rocket Engines," *Journal of Propulsion and Power*, vol. 18, May. 2002, pp. 600-609.
- [3] S. Yuasa, K. Yamamoto, H. Hachiya, K. Kitagawa, and Y. Oowada, "Development of a Small Sounding Hybrid Rocket with a Swirling-Oxidizer-Type Engine," *37th AIAA/ASME/SAE/ASEE Joint Propulsion Conference and Exhibit*, Salt Lake City (Utah): AIAA, 2001.
- [4] J.R. Caravella, S.D. Heister, and E.J. Wernimont, "Characterization of Fuel Regression in a Radial Flow Hybrid Rocket," *Journal of Propulsion and Power*, vol. 14, 1998, pp. 51-56.
- [5] M.A. Karabeyoglu, G. Zilliac, B.J. Cantwell, S. De Zilwa, and P. Castelluci, "Scale-up Tests of High Regression Rate Liquefying Hybrid Rocket," *41st AIAA/ASME/SAE/ASEE Joint Propulsion Conference & Exhibit*, Reno (Nevada): AIAA, 2003.
- [6] S.R. Jain and G. Rajendran, "Performance parameters of some new hybrid hypergols," *Journal of Propulsion and Power*, vol. 1, Nov. 1985, pp. 500-502.
- [7] M.C. Ventura and H. S.D., "Hydrogen Peroxide as an Alternate Oxidizer for a Hybrid Rocket Booster," *Journal of Propulsion and Power*, vol. 11, Jan. 1995, pp. 562-565.
- [8] K. Lohner, J. Dyer, E. Doran, Z. Dunn, and G. Zilliac, "Fuel Regression Rate Characterization Using a Laboratory Scale Nitrous Oxide Hybrid Propulsion System," *AIAA*, 2006.
- [9] A. McCormick, E. Hultgren, M. Lichtman, J. Smith, R. Sneed, and S. Azimi, "Design, Optimization, and Launch of a 3" Diameter N₂O/Aluminumized Paraffin Rocket," *AIAA*.
- [10] E.E. Rice and D.J. Gramer, "Methane and Methane/Aluminium Cryogenic Hybrid Rocket Engines," *38th Aerospace Sciences Meeting & Exhibit*, Reno (Nevada): AIAA, 2000.
- [11] G.A. Risha, A. Ulas, E. Boyer, S. Kumar, and K.K. Kuo, "Combustion of HTPB-Based Solid Fuels Containing Nano-sized Energetic Powder in a Hybrid Rocket Motor," *37th AIAA/ASME/SAE/ASEE Joint Propulsion Conference and Exhibit*, Salt Lake City (Utah): AIAA, 2001.
- [12] F. Martin, A. Chapelle, O. Orlandi, and P. Yvart, "Hybrid propulsion systems for future space applications," Nashville (Tennessee): AIAA, 2010.
- [13] T.P. Wampler, ed., *Applied Pyrolysis Handbook*, CRC Press, 2006.

- [14] A. Nemeth, M. Blazso, P. Baranyai, and T. Vidoczy, "Thermal degradation of polyethylene modeled on tetracontane," *Journal of Analytical and Applied Pyrolysis*, vol. 81, Mar. 2008, pp. 237-242.
- [15] S.E. Levine and L.J. Broadbelt, "Detailed mechanistic modeling of high-density polyethylene pyrolysis: Low molecular weight product evolution," *Polymer Degradation and Stability*, vol. 94, May. 2009, pp. 810-822.
- [16] G.P. Smith, D.M. Golden, M. Frenklach, N.W. Moriarty, B. Eiteneer, M. Goldenberg, T.C. Bowman, R.K. Hanson, S. Song, W.C.J. Gardiner, V.V. Lissianski, and Z. Qin, "Grimech 3.0," http://www.me.berkeley.edu/gri_mech/.
- [17] P. Dagaut and M. Cathonnet, "The ignition, oxidation, and combustion of kerosene: A review of experimental and kinetic modeling," *Progress in Energy and Combustion Science*, vol. 32, 2006, pp. 48-92.
- [18] G. Cai and H. Tian, "Numerical Simulation of the Operation Process," *42nd AIAA/ASME/SAE/ASEE Joint Propulsion Conference & Exhibit*, Sacramento (California): AIAA, 2006.
- [19] N. Serin and Y.A. Göğüş, "A Fast Computer Code for Hybrid Motor Design, EULEC and Results Obtained for HTPB/O₂ Combination," *39th AIAA/ASME/SAE/ASEE Joint Propulsion Conference and Exhibit*, Huntsville (Alabama): AIAA, 2003.
- [20] M. Stoia-Djeska and F. Mingireanu, "A Computational Fluid Dynamics Based Stability Analysis For Hybrid Rocket Motor Combustion," *16th AIAA/CEAS Aeroacoustics Conference*, AIAA, 2010.
- [21] H.-J. Kim and Y.-M. Kim, "Numerical modeling for combustion processes of hybrid rocket engine," *37th AIAA/ASME/SAE/ASEE Joint Propulsion Conference and Exhibit*, Salt Lake City (Utah): AIAA, 2001.
- [22] K. Yoshimura and K. Sawada, "Numerical Simulation of Swirling Flowfield in Combustion Chamber for Hybrid Rocket Engine," *48th AIAA Aerospace Sciences Meeting Including the New Horizons Forum and Aerospace Exposition*, Orlando (Florida): AIAA, 2010.
- [23] A. Antoniou, "A physics-based two-dimensional comprehensive mathematical model to predict non-uniform regression rate in solid fuels for hybrid rocket motors," New Orleans University, 2005.
- [24] K. Akyuzlu, R. Kagoo, and A. Antoniou, "A Physics Based Mathematical Model to Predict the Regression Rate in an Ablating Hybrid Rocket Solid Fuel," *37th AIAA/ASME/SAE/ASEE Joint Propulsion Conference and Exhibit*, Salt Lake City (Utah): 2001.
- [25] A. Antoniou and K.M. Akyuzlu, "A Physics Based Comprehensive Mathematical Model to Predict Motor Performance in Hybrid Rocket Propulsion Systems," *41st AIAA/ASME/SAE/ASEE Joint Propulsion Conference & Exhibit*, Tucson (Arizona): AIAA, 2005.
- [26] K.M. Akyuzlu, A. Antoniou, and M.W. Martin, "Determination of Regression Rate in an Ablating Hybrid Rocket Solid Fuel Using a Physics Based Comprehensive Mathematical Model," *38th AIAA/ASME/SAE/ASEE Joint Propulsion Conference & Exhibit*, Indianapolis (Indiana): AIAA, 2002.
- [27] Y.-xin Yang, C.-bo Hu, T.-min Cai, and D.-chuan Sun, "Instantaneous Regression Rate Computation of Hybrid Rocket Motor Bases on Fluid-Solid Coupling Technique," *43rd AIAA/ASME/SAE/ASEE Joint Propulsion Conference & Exhibit*, Cincinnati (Ohio): AIAA, 2007.
- [28] G. Gariani, F. Maggi, and L. Galfetti, "Simulation Code for Hybrid Rocket Combustion," *46th AIAA/ASME/SAE/ASEE Joint Propulsion Conference & Exhibit*, Nashville (Tennessee): AIAA, 2010.
- [29] N. Gascoin and P. Gillard, "Preliminary pyrolysis and combustion study for the hybrid propulsion," *46th AIAA/ASME/SAE/ASEE Joint Propulsion Conference & Exhibit*, Nashville (Tennessee): AIAA, 2010.
- [30] J.H. Ferziger and M. Peric, *Computational Methods for Fluid Dynamics*, 2002.
- [31] K.K. Kuo, *Principles of Combustion*, John Wiley & sons, Inc., 2005.
- [32] D.G. Goodwin, "An Open-Source, Extensible Software Suite for CVD Process Simulation," *Chemical Vapor Deposition XVI and EUROCVI 14*, vol. 2003-08, pp. 155-162 (2003).
- [33] A. Faghri, A.F.Y.Z.J. Howell, Y. Zhang, and J. Howell, *Advanced Heat and Mass Transfer*, Global Digital Press, 2010.
- [34] J. Gosse, "Mécanique des fluides," *Techniques de l'ingénieur*, vol. A 1 870, pp. 1-57.
- [35] U. Ghia, K.N. Ghia, and C.T. Shin, "High-Re solutions for incompressible flow using the Navier-Stokes equations and a multigrid method," *Journal of Computational Physics*, vol. 48, 1982, pp. 387-411.
- [36] G.A. Sod, "A survey of several finite difference methods for systems of nonlinear hyperbolic conservation laws," *Journal of Computational Physics*, vol. 27, Apr. 1978, pp. 1-31.